Electronic Supplementary Material (ESI) for Journal of Materials Chemistry A.

Energy Storage Mechanisms in Vacancy-Ordered Wadsley–Roth Layered Niobates

Kit McColl,[†] Kent J. Griffith,[‡] Rebecca L. Dally,[¶] Runze Li,[§] Jason E. Douglas,[‖] Kenneth R. Poeppelmeier,[‡] Furio Corà,[†] Igor Levin,[⊥] and Megan M. Butala[*,§,⊥]

†*Department of Chemistry, University College London, London, WC1H 0AJ, UK*

‡*Department of Chemistry, Northwestern University, Evanston, IL 60208, USA.*

¶*NIST Center for Neutron Research, National Institute of Standards and Technology, Gaithersburg, MD 20899, USA.*

§*Department of Materials Science and Engineering, University of Florida, Gainesville, FL 32611, USA.*

‖*Materials Science and Engineering Division, National Institute of Standards and Technology, Gaithersburg, MD 20899, USA.*

⊥*Materials Measurement Science Division, National Institute of Standards and Technology, Gaithersburg, MD 20899, USA.*

E-mail: mbutala@ufl.edu

Supporting Information

Additional information on Rietveld Refinement before Cycling

An instrumental parameter file, based on NIST SRM 660a LaB_6 with a Thompson-Cox-Hastings pseudo-Voigt Axial divergence asymmetry peak profile, was used during refinement to provide access to microstructural information using the integral breadth method. Data from 11-BM do not typically require low-angle peak asymmetry corrections due to the instrumental profile, however, the first Bragg peaks for KNb_3O_8 and $NaNb_3O_8$ are both intense and at quite a low angle ($2\theta \approx 2.2^\circ$), and a small asymmetry correction was needed for $2\theta \leq 3^\circ$. Values in parenthesis in Tables S1 and S2 represent plus and minus one standard deviation confidence intervals.

KNb_3O_8 before cycling

The Bragg peak width due to the sample was found to be anisotropic as a function of momentum transfer, Q. This was evident during initial analysis using isotropic size and strain parameters, which did not capture peak profile shapes. The data was much better captured using an anisotropic size broadening model based on linear combinations of spherical harmonics and an additional isotropic strain parameter (contributing to the Lorentzian line shape). Refined parameters are reported in Table S1, and an extended view of the fitted profile relative to that in the main text is shown in Figure S1.

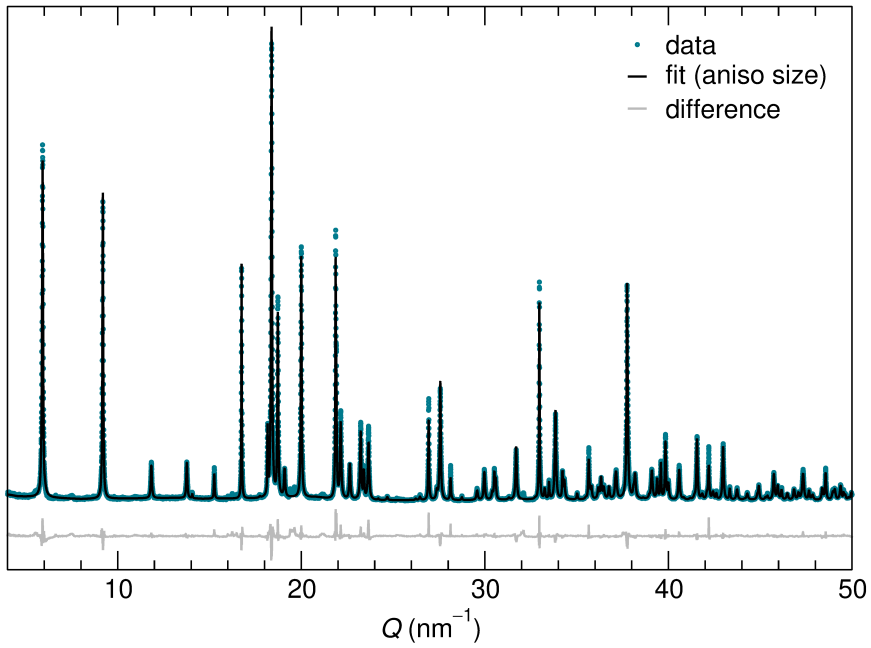

Figure S1: Expanded view of KNb_3O_8 11-BM XRD data (points) and calculated fit (lines) using isotropic strain and anisotropic size broadening.

Table S1: Fit parameters from the Rietveld refinement of KNb_3O_8 11-BM XRD data using isotropic strain, anisotropic size broadening, and a low Q anisotropic peak shape parameter.

KNb_3O_8 ($Amam$), R_p = 10.2, R_{wp} = 12.1, χ^2 = 1.884							
a = 8.93412(1) Å		b = 21.24121(4) Å		c = 3.811553(4) Å			
Atom	x	y	z	B_{11}	B_{22}	B_{33}	B_{23}
Nb	0.94018(3)	0.368190(15)	0	0.00132(3)	0.000354(6)	0.0046(2)	0.00009(2)
Nb	$\frac{1}{4}$	0.24165(2)	0	0.00128(5)	0.00030(1)	0.0029(3)	n/a
K	$\frac{1}{4}$	0.98530(6)	0	0.0069(2)	0.00086(3)	0.0174(8)	n/a
O	0.4098(2)	0.15725(9)	0	0.0019(3)	0.00137(9)	0.015(2)	−0.0001(1)
O	0.0609(4)	0.43049(9)	0	0.0103(4)	0.00052(7)	0.024(2)	−0.0013(1)
O	0.0934(2)	0.29520(10)	0	0.0050(3)	0.00097(8)	0.018(2)	−0.0004(1)
O	$\frac{1}{4}$	0.71350(14)	0	0.0066(6)	0.0006(1)	0.020(3)	n/a
O	$\frac{1}{4}$	0.58600(13)	0	0.0051(5)	0.00037(9)	0.012(2)	n/a
Isotropic strain							
X^a	0.1084(5)						
$Max. strain$	0.0743%						

[a]Lorentzian broadening parameter

$NaNb_3O_8$ before cycling

Similar to KNb_3O_8, peak broadening in high resolution XRD data was found to originate from a combination of strain and anisotropic particle size. Several regions containing large impurity peaks were excluded from the refinement. However, smaller contributions at other Q values could not be accounted for and could contribute to the integral breadth values of peaks (if a small impurity reflection was at the same position), which added complexity in the strain and particle size analysis for this data.

Isotropic strain and anisotropic size broadening were clearly coupled, and so were refined sequentially, rather than simultaneously. The results of the refinement are provided in Table S2.

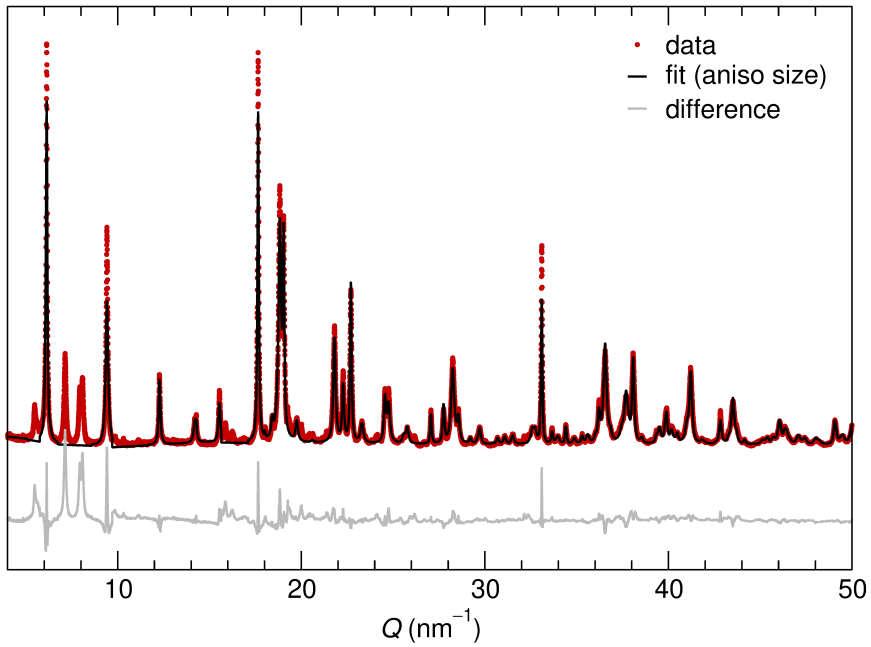

Figure S2: Expanded view of $NaNb_3O_8$ 11-BM XRD data (points) and calculated fit (lines) using isotropic strain and anisotropic size broadening, which shows several yet unidentified impurities.

Table S2: Fit parameters from the Rietveld refinement of $NaNb_3O_8$ 11-BM XRD data using isotropic strain, anisotropic size broadening, and a low Q anisotropic peak shape parameter. ([a] Lorentzian broadening parameter, [b] Gaussian broadening parameter)

$NaNb_3O_8$ ($PmnmZ$), R_p = 16.1, R_{wp} = 17.6, χ^2 = 3.34				
a = 8.80113(5) Å		b = 10.23304(7) Å		c = 3.79658(2) Å
Atom	x	y	z	B_{iso}
Nb	0.94253(6)	0.74913(7)	$\frac{1}{4}$	0.591(8)
Nb	$\frac{1}{4}$	0.48018(7)	$\frac{1}{4}$	0.40(1)
Na	$\frac{1}{4}$	0.9298(4)	$\frac{3}{4}$	0.93(7)
O	0.4159(4)	0.3026(4)	$\frac{1}{4}$	0.79(4)
O	0.0753(5)	0.8798(4)	$\frac{1}{4}$	0.79(4)
O	0.0899(4)	0.5918(4)	$\frac{1}{4}$	0.79(4)
O	$\frac{1}{4}$	0.4106(5)	$\frac{3}{4}$	0.79(4)
O	$\frac{1}{4}$	0.1601(5)	$\frac{3}{4}$	0.79(4)
Isotropic strain				
X^a	0.175(2)			
U^b	0.033(1)			
$Max. strain$	0.1737%			

Additional characterization data

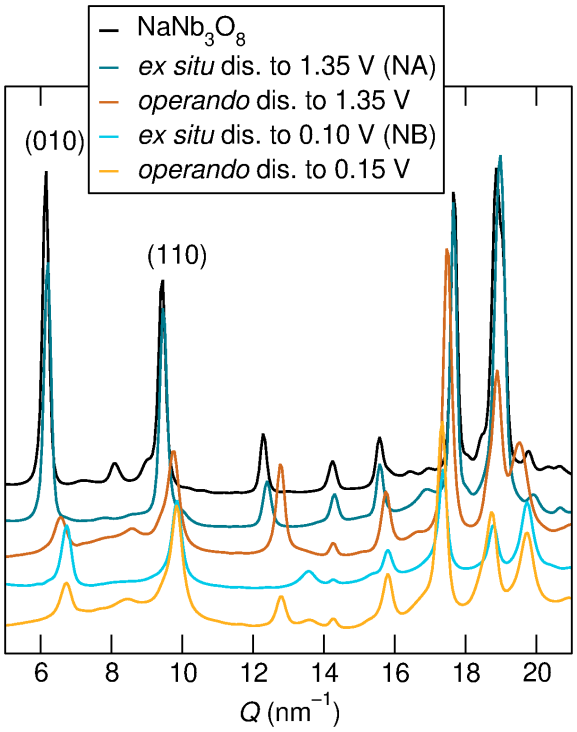

Figure S3: *Ex situ* synchrotron X-ray scattering from $NaNb_3O_8$ before and after cycling to various states of charge. Plotted together, this data highlights the negligible change of the (010) peak position upon *ex situ* discharge to about $LiNaNb_3O_8$, where as the analogous *operando* discharge to the same potential and composition shows a shift of the same peak to higher Q. This also shows that upon complete discharge, the *ex situ* and *operando* average structures are similar to one another. (Intensity differences between the same reflections in *ex situ* and *operando* data is a result of preferred orientation in the *operando* cell.)

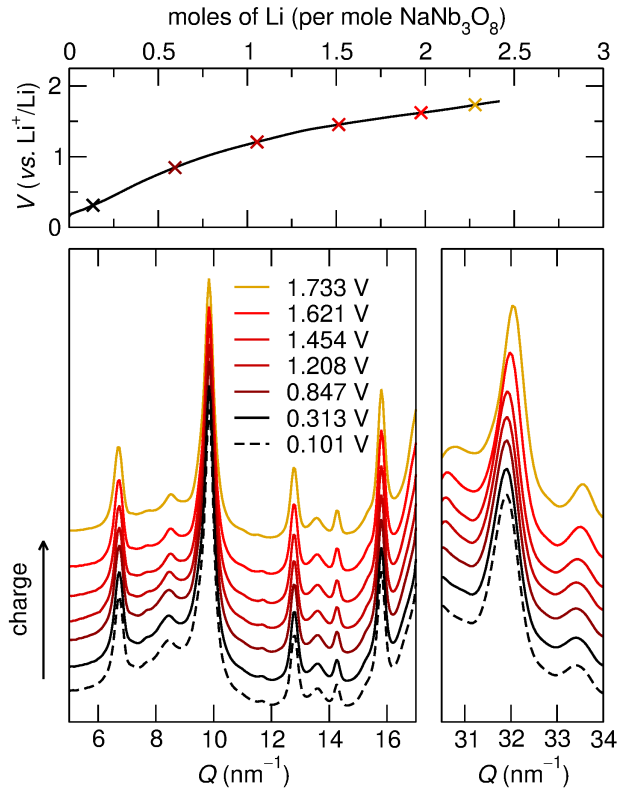

Figure S4: *Operando* synchrotron X-ray scattering over part of the first charge of $NaNb_3O_8$ following discharge to 0.1 V shows negligible evolution of the average structure.

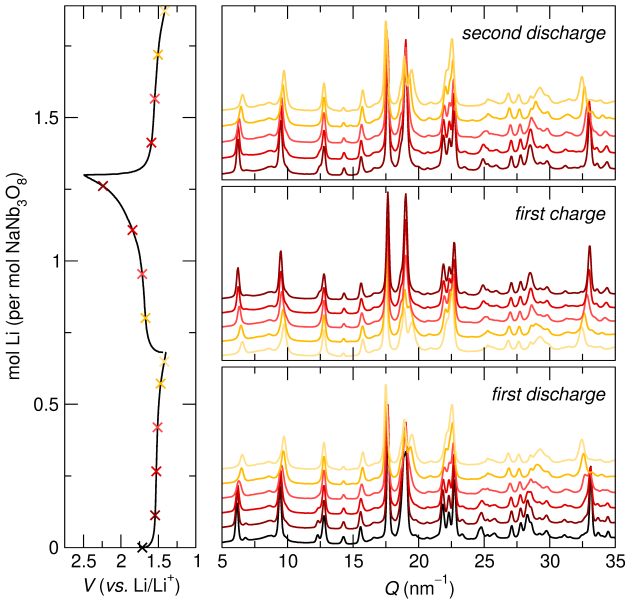

Figure S5: *Operando* synchrotron X-ray scattering over 1.5 cycles of $NaNb_3O_8$ in a narrow potential range over just the high potential plateau. This shows improved reversibility of lithiation and average structure evolution.

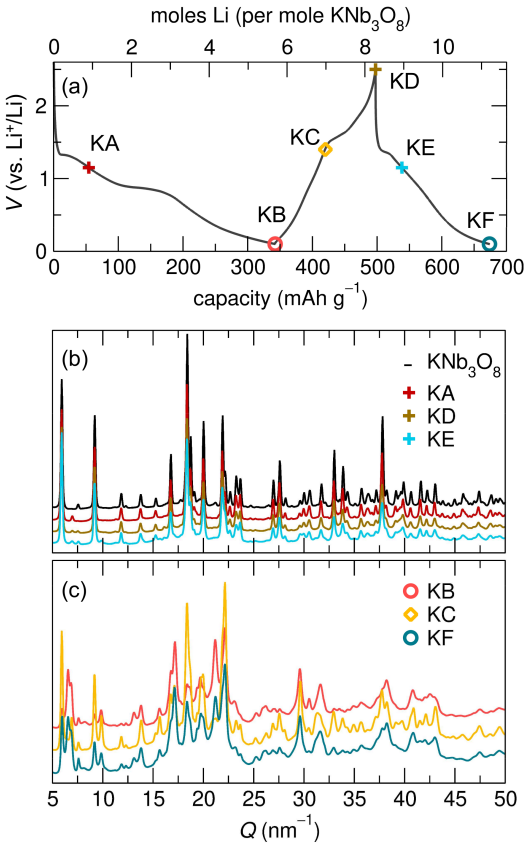

Figure S6: (a) Representative 1.5 cycles of KNb_3O_8, with symbols and labels at various states of charge. At each state of charge, (b and c) *ex situ* synchrotron XRD shows the evolution of average structure features. In (b), KNb_3O_8 and states of charge that resembled it in *ex situ* characterization are grouped together. In (c), discharge products and the states of charge with similar average structure are grouped together.

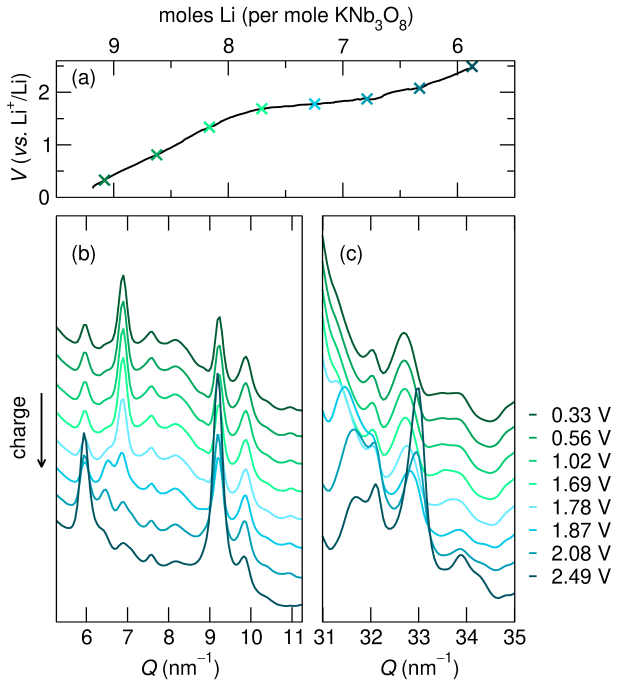

Figure S7: (a) The *operando* charge profile of KNb_3O_8 following discharge to 0.1 V and (b and c) the corresponding synchrotron XRD data at each state of charge. XRD shows (b) a partial recovery of the 020 reflection intensity at its original position, and (c) a shift of the 002 reflection toward its original position.

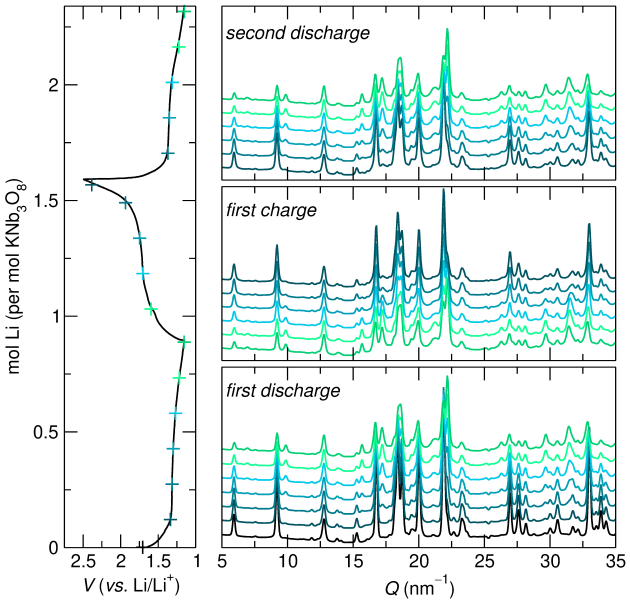

Figure S8: *Operando* synchrotron X-ray scattering over 1.5 cycles of KNb_3O_8 in a narrow potential range over just the high potential plateau. This shows improved reversibility of lithiation and average structure evolution.

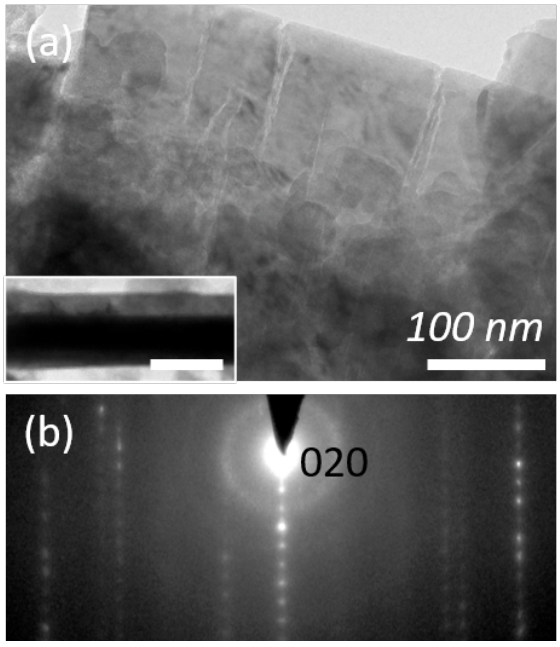

Figure S9: Bright-field TEM image of a crystallite after the first discharge to 0.1 V. The inset shows the same crystallite tilted by nearly 90° to bring the [010] layer-stacking direction into the image plane (the crystallite is now about 400 nm thick along the beam direction, the scale par is 100 nm). (b) Selected-area electron diffraction recorded in this edge-on orientation reveals discrete $0k0$ spots, which suggest an ordered tacking sequence. Minor diffuse streaking appears to be associated with the side surfaces of the platelet.

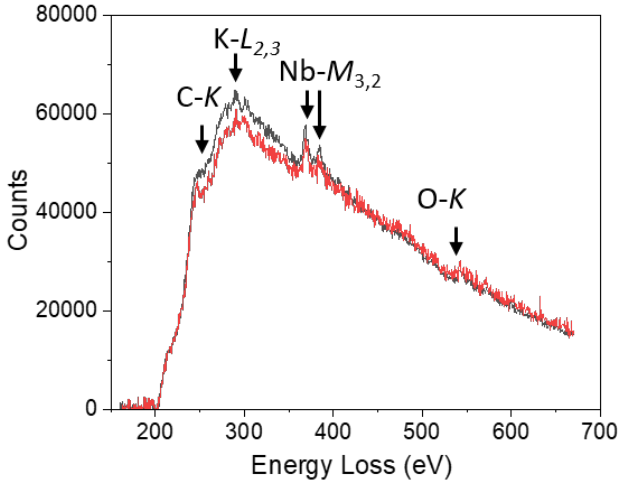

Figure S10: *Ex situ* background-subtracted EELS spectra recorded (in STEM mode) from the adjacent crystalline (black) and amorphous-contrast (red) areas in a single platelet of KNb_3O_8 discharged to 0.1 V, as in Figure 19 in the main text. The presence of K, Nb, and O in both spectra is evident. A significant contribution of the C K-edge to the spectra can be attributed to the conductive carbon additive in the composite electrode.

Additional information on NMR data and analysis

NMR Conventions

In this study, the Haeberlen convention is used to describe the chemical shift tensor with the isotropic shift $\delta_{iso} = (\delta_{11} + \delta_{22} + \delta_{33})/3$; chemical shift anisotropy $\delta_{CSA} = \delta_{33} - \delta_{iso}$; and the shift asymmetry $\eta_{CSA} = \frac{\delta_{22}-\delta_{11}}{\delta_{33}-\delta_{iso}}$.[1–3] In this definition, the principal components of the shift tensor are ordered such that $|\delta_{33} - \delta_{iso}| \geq |\delta_{11} - \delta_{iso}| \geq |\delta_{22} - \delta_{iso}|$. The above definition of δ_{CSA} is sometimes referred to as the reduced anisotropy, which is equal to 2/3 of the 'full' anisotropy $\Delta\delta = \delta_{33} - (\delta_{11} + \delta_{22})/2$ used by some authors and programs. The quadrupolar coupling constant, C_Q, is defined by the nuclear quadrupole moment, Q (not momentum transfer as in some X-ray diffraction plots elsewhere), and the largest principal component V_{33} of the EFG at the nucleus according to $C_Q = \frac{eQV_{33}}{h}$, where e is the electric charge and h is Planck's constant. The quadrupolar asymmetry parameter η_Q is defined by the EFG tensor components as $\eta_Q = \frac{V_{11}-V_{22}}{V_{33}}$, with components ordered such that $|V_{33}| \geq |V_{22}| \geq |V_{11}|$. The relative orientations of the chemical shift and quadrupolar tensors are defined by a set of Euler angles α, β, and γ defined here in the (ZYZ) Rose convention.

Table S3: Calculated ^{23}Na and ^{93}Nb NMR parameters for $NaNb_3O_8$ and KNb_3O_8. (*The calculated ^{23}Na shielding was 564 ppm, but previous studies[4] have shown ^{23}Na shielding to be less reliable than for other nuclei, so a conversion to shift was not performed. Regardless, there is no ambiguity here as there is only one ^{23}Na site present in $NaNb_3O_8$.)

Site	Wyckoff	Shift Tensor			Shielding Tensor		Euler Angles		
	Symbol	δ_{iso} (ppm)	CSA	η_{CS}	C_Q (MHz)	η_Q	α (°)	β (°)	γ (°)
$NaNb_3O_8$									
Na(1)	2b	n/a*	8.5	0.59	−1.36	0.18	0	90	0
Nb(1)	4e	−1061	−580	0.21	−47.3	0.47	0	22	0
Nb(2)	2a	−1165	110	0.88	19.1	0.74	1	0	90
KNb_3O_8									
Nb(1)	8f	−1080	−540	0.18	−41.3	0.44	0	9	0
Nb(2)	4c	−1164	−130	0.97	−18.9	0.53	90	90	90

Table S4: Experimental ^{23}Na and ^{93}Nb NMR parameters for $NaNb_3O_8$ and KNb_3O_8. The calculated parameters of Table S3 were used as initial guesses and then refined by comparing the goodness-of-fit of the calculated lineshapes to experimental spectra. Estimated uncertainty in the last digit(s) of each parameter derived from the fits are given in parentheses. Calculated Euler angles were used without refinement to minimize the number of variables in the fits. (*These relatively small shift anisotropies did not significantly affect the fit, so the calculated values were used directly without refinement and thus without error estimation.)

Site	Wyckoff Symbol	Shift Tensor δ_{iso} (ppm)	CSA	η_{CS}	Shielding Tensor $\pm C_Q$ (MHz)	η_Q
$NaNb_3O_8$						
Na(1)	$2b$	$-13.9(2)$	8.5	0.59	0.52(5)	0.9(1)
Nb(1)	$4e$	$-1040(40)$	$-580(100)$	0.2(2)	40(2)	0.3(1)
Nb(2)	$2a$	$-1140(30)$	115*	0.88*	17(2)	0.5(2)
KNb_3O_8						
Nb(1)	$8f$	$-1060(40)$	$-540(100)$	0.2(2)	37(2)	0.3(1)
Nb(2)	$4c$	$-1180(30)$	-132*	0.97*	20(1)	0.6(2)

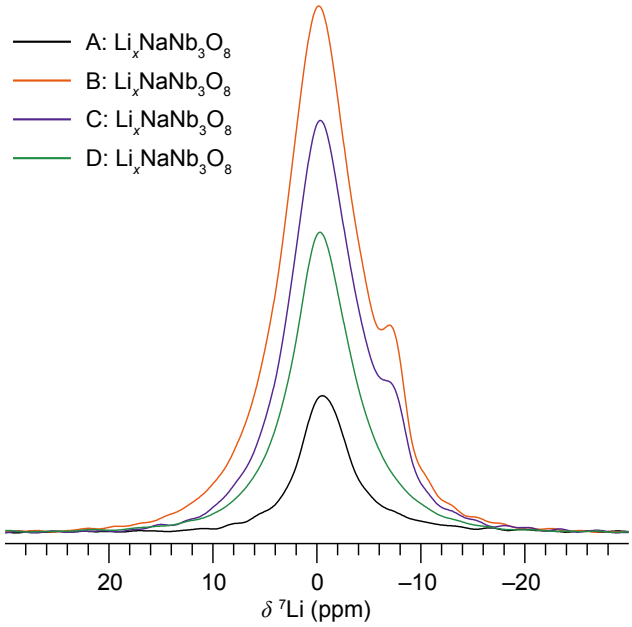

Figure S11: The analysis of *ex situ* ^{7}Li MAS NMR of $Li_xNaNb_3O_8$ at various states of charge yielded quantitative determination of Li content. These values are provided in Table S5, scaled based on electrochemical measurements at high potential during which there were not side reactions, and by doing such, a reasonable estimate of x is achieved.

Table S5: Table of quantitative Li compositions (relative) from *ex situ* ^{7}Li MAS NMR at various states of charge were derived from the data in Figure S11. Those values were normalized by the Li content (per mol $NaNb_3O_8$) from electrochemical cell NA, which was cycled to 1.4 V and so had no significant side reactions to contribute to the measured Li content. from this, the "normalized" content is used as the actual x for $Li_xNaNb_3O_8$ and the "difference" is the Li content measured in electrochemical cycling associated with side reactions.

	Li composition			
	from NMR (relative)	from cycling (per mol $NaNb_3O_8$)	normalized (NMR $\times$ 0.71 $\div$ 0.14)	difference (side reactions)
$NaNb_3O_8$	*n/a*	0	*n/a*	0
NA	**0.14**	**0.71**	0.71	0
NB	1.00	7.98	5.07	2.91
NC	0.69	5.86	3.50	2.36
ND	0.43	3.84	2.18	1.60

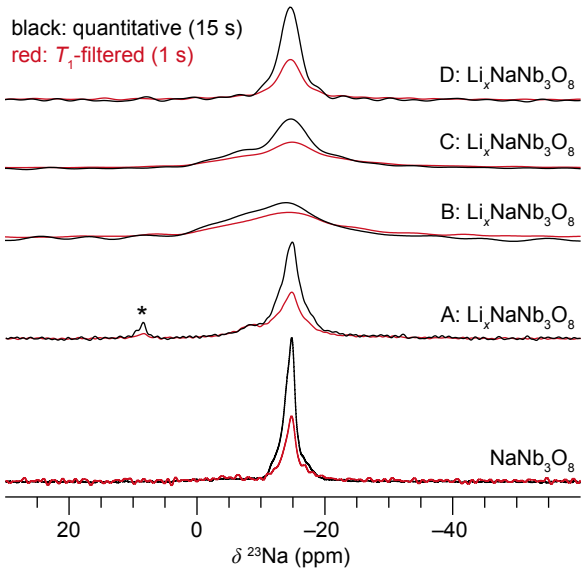

Figure S12: Evolution of the *ex situ* ^{23}Na MAS spectrum of $Li_xNaNb_3O_8$ at various states of charge at absolute intensities rather than normalized (sample labels correspond to the cycling and XRD data in Figure 8 in the main text). An impurity from sample preparation is denoted with an asterisk.

Additional information for the DFT calculations.

Basis sets

All-electron atom-centered Gaussian basis sets were used for all atoms, available from the CRYSTAL online database (www.crystal.unito.it), indicated by the following labels online: Na [Na_8-511(1d)G_baranek_2013_NaNbO3], Nb [Nb_986-31(631d)G_dallolio_1996], O [O_8-411d1_cora_2005], Li [Li_5-11(1d)G_baranek_2013_LiNbO3].

Calculations of migration barriers using constrained geometry optimisations

The activation barriers for Li migration were determined using constrained geometry optimisations. The first step taken was the optimisation of the initial and final geometries of the ions along the migration pathway. Subsequently, a linear interpolation of the coordinates of the diffusing ion between the two sites was manually calculated leading to a set of images. Initially 5 images were chosen for pathways 1, 2 and 3 under dilute conditions, not including the initial and final geometries. These images were independently relaxed, under the condition that movement of the migrating Li was constrained in the direction of motion. To prevent the entire structure moving with the mobile Li, a single additional ion, chosen to be the closest O-ion to the migrating ion in its starting geometry, had its movement constrained. The energies of the points along the pathway were then calculated relative to the initial or final geometry. This method allows for a finer interpolation of points along the pathway to be subsequently applied if the position or energy of the activation barrier is not evident. A finer interpolation of points was required for pathway 2, totalling 6 images along the pathway. During the initial relaxations of the images along pathway 3 (from Y to Y'), it became evident that there were intermediate sites (Z and Z'). To obtain the full migration profile along path 3, points Z were independently fully

relaxed, and new interpolations were made between Y and Z, Z and Z', and Z' and Y, each consisting of five images.

Square-planar 'W' sites

In addition to the X, Y and Z sites, we identified another metastable Li^+ insertion site, labelled 'W' (Figure S13). W sites are located in the square channels and Li-ions in the sites adopt square-planar geometry. The W sites must be reached by diffusion down the square channels, via X to W hops. These hops have an activation barrier of 1.04 eV, making them highly unfavourable compared to diffusion in the interlayer space under dilute conditions, or 'cross-block' hops. In other WR-type materials, such as $TiNb_2O_7$, $Nb_{12}WO_{33}$ and $Nb_{14}W_3O_{44}$, equivalent 'pocket' to 'window' hops have activation barriers of ≈ 0.4 eV.[5,6] The higher activation barrier for the pathway in $NaNb_3O_8$ can be attributed to the presence of Na ions between the layers that partially block the square channels. Due to the high activation barrier to access them, and the high energy of W sites, we predict that they are not occupied by Li cycling.

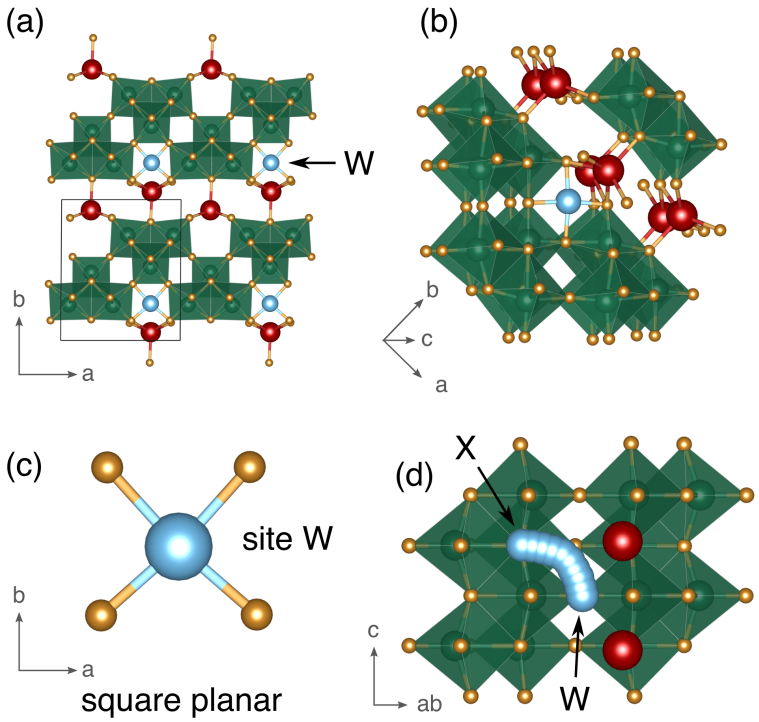

Figure S13: Geometry of Li^+ ions in square-planar window 'W' sites. (a) View along the c direction, showing Li^+ in a square-planar geometry in the square channels. (b) Projected view of the structure showing the position between two Na^+ ions along the c direction. (c) Detail of the near-symmetric square-planar geometry. (d) Detail of the migration pathway from pocket X sites to W sites, indicating the movement past Na^+.

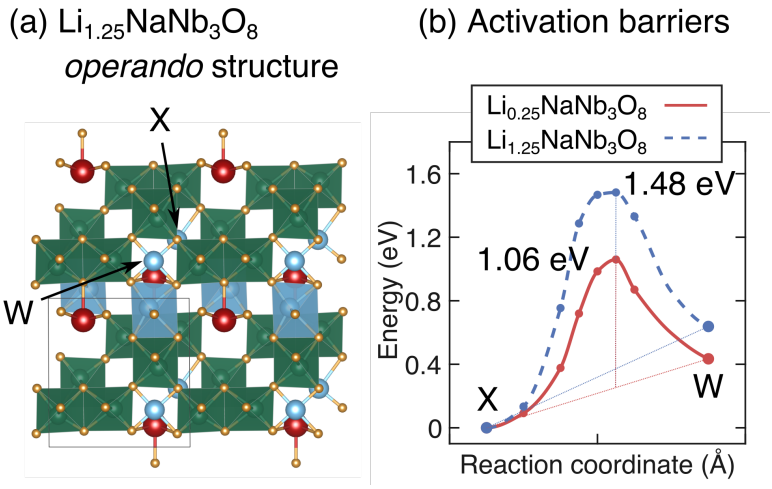

Figure S14: Li^+ diffusion along square channels when Y sites are filled at a composition of $LiNaNb_3O_8$.

References

(1) Slichter, C. P. *Principles of Magnetic Resonance*; Springer Berlin Heidelberg: Berlin, Heidelberg, 1978; pp 252–274.

(2) Sternhell, S. M. Mehring. Principles of High Resolution NMR in Solids. Springer-Verlag, Berlin, Heidelberg, New York, 1983. 342 pp. Cloth $71.80. ISBN 3-540-11852-7. *Org. Magn. Res.* **1983**, *21*, 770–770.

(3) Drakenberg, T. Alois Steigel and Hans Wolfgang spiess. NMR basic principles and progress, volume 15, dynamic NMR spectroscopy. Edited by P. Diehl, E. Fluck and R. Kosfeld, Springer Verlag, Berlin, 1978. *Org. Magn. Res.* **1979**, *12*, iv–iv.

(4) Xu, J.; Lucier, B. E. G.; Lin, Z.; Sutrisno, A.; Terskikh, V. V.; Huang, Y. New Insights into the Short-Range Structures of Microporous Titanosilicates as Revealed by $^{47/49}$Ti, ^{23}Na, ^{39}K, and ^{29}Si Solid-State NMR Spectroscopy. *J. Phys. Chem. C* **2014**, *118*, 27353–27365.

(5) Griffith, K. J.; Seymour, I. D.; Hope, M. A.; Butala, M. M.; Lamontagne, L. K.; Preefer, M. B.; Koçer, C. P.; Henkelman, G.; Morris, A. J.; Cliffe, M. J.; Dutton, S. E.; Grey, C. P. Ionic and Electronic Conduction in $TiNb_2O_7$. *J. Am. Chem. Soc.* **2019**, *141*, 16706–16725.

(6) Koçer, C. P.; Griffith, K. J.; Grey, C. P.; Morris, A. J. Lithium Diffusion in Niobium Tungsten Oxide Shear Structures. *Chem. Mater.* **2020**, *32*, 3980–3989.